Comparisons of Four Methods for Tropical Cyclone Center Detection in a High-Resolution SimulationComparisons of Four Methods for Tropical Cyclone Center Detection in a High-Resolut…

Article *in* Journal of the Meteorological Society of Japan · January 2020

DOI: 10.2151/jmsj.2020-020

3 authors, including:

Huadong Yang
Nanjing Institute of Atmospheric Sciences
2 PUBLICATIONS **1** CITATION

Journal of the Meteorological Society of Japan

EARLY ONLINE RELEASE

The DOI for this manuscript is
DOI:10.2151/jmsj.2020-020
J-STAGE Advance published date: January 22nd 2020

Comparisons of Four Methods for Tropical Cyclone Center Detection in a High-Resolution Simulation

Huadong Yang[1], Liguang Wu[2], and Tong Xie[1]

[1] Key Laboratory of Meteorological Disaster of Ministry of Education, Nanjing University of Information Science and Technology, Nanjing, China

[2]Department of Atmospheric and Oceanic Sciences and Institute of Atmospheric Sciences, Fudan University, Shanghai, China

November 21, 2019

Revised for *Journal of the Meteorological Society of Japan*

Corresponding author address: Dr. Liguang Wu

Department of Atmospheric and Oceanic Sciences & Institute of Atmospheric Sciences

Fudan University, Shanghai 200438, China

E-mail: liguangwu@fudan.edu.cn

Abstract

The tropical cyclone (TC) center position is often needed in the study of the inner-core processes although there is currently no consensus on the definition of the TC center. While previous studies evaluated center-detecting methods in terms of the center position, vertical tilt and decomposed symmetric and asymmetric circulations, this study used the 1-km resolution output of the predicted Hurricane Wilma (2005) at 5-minute intervals to evaluate the four TC centers that are frequently used in the diagnostic analysis of the inner-core dynamics processes: the pressure centroid center (PCC), the potential vorticity (PV) centroid center (PVC), the maximum tangential wind center (MTC) and the minimum pressure variance center (MVC) by focusing on the evolution of the small-scale track oscillation and vortex tilt.

The differences in the detected center position and vertical tilt are generally small during the course of rapid intensification and eyewall replacement. The four methods all lead to similar small-scale track oscillations that rotate cyclonically around the mean track. While the MVC and PVC lead to a relatively smooth rotation, abrupt changes exist in the track oscillation of the MTC; the track oscillation of the PCC contains amplified embedded rotations that are associated with the PV mixing in the eye region. The tracks of the MVC and PVC relative to the lower-level center (vertical tilt) are generally smooth, while the relative tracks of the MTC and PCC contain abrupt changes. The MVC also leads to the strongest symmetric structure in the tangential wind, PV, and radial PV gradient in the eyewall region. This study suggests that the MVC should be selected in the study of inner-core processes.

1. Introduction

Advances in numerical models and computational capability have made it possible to simulate inner-core processes of the tropical cyclone (TC) with the grid spacing less than 1 km (e.g., Zhu 2008; Rotunno et al. 2009; Bryan et al. 2014; Stern and Bryan 2018; Rotunno and Bryan 2014; Green and Zhang 2015). The inner-core processes have significant implications to the dynamics of structure and intensity changes (Schubert et al. 1999; Kossin and Schubert 2001). For example, the instability of vortex Rossby waves and PV mixing are closely associated with the radial gradient of the symmetric component of potential vorticity (PV) with respect to the TC center (Montgomery and Kallenbach 1997; Schubert et al. 1999; Kossin and Schubert 2001). It has been long known that the accuracy of decomposed symmetric and asymmetric components of the TC circulation depends critically on the TC center position due to strong wind speed and the associated strong radial gradient in the inner core region (Willoughby 1992). Although various methods have been used in previous numerical studies (e. g., Jones 1995; Frank and Richie 1999; Braun et al. 2006; Nguyen et al. 2014; Ryglicki and Hart 2015), there is no consensus on the detection of the TC center.

Nguyen et al. (2014) examined the performance of center-detecting methods by simulating the rapid intensification of Tropical Storm Gabrielle (2001) with the finest horizontal grid spacing of 1 km. After comparing the four methods, i.e., the centroid of PV (Reasor and Montgomery 2001), the centroid of pressure, the location that maximizes the azimuthally averaged wind speed (Reasor et al. 2013), and the location that maximized the low-level circulation (Cavallo et al. 2013), they found that the

pressure centroid outperformed the methods identified with the other three methods in terms of the center position relative to storm-scale cyclonic flow, track smoothness on an hourly time scale, vertical coherence of the vortex tilt, and sensitivity to the model horizontal resolution. They argued that the good performance of the pressure centroid was attributed to the smoothing effect of the pressure field, while there are localized high-amplitude convective features in the vorticity and PV. Nguyen et al. (2014) also evaluated the maximum circulation method and found that the identified center exhibits an unrealistic tilt in the vertical. Nguyen et al. (2014) argued that the performance of the minimum pressure variance method proposed in Braun (2002) and Braun et al. (2006) is similar to the pressure centroid method.

Ryglicki and Hart (2015) conducted a comprehensive review on the center-detecting methods in observational and numerical studies and classified the existing methods into three categories. The first is called the local extreme (LE) category, in which the maximum or minimum value of a given field is detected in the inner-core region. The LE methods work mainly for the simulation with the horizontal spacing of ~10 km. Jones (1995) defined the position of the minimum height and the maximum PV as the TC center, while Frank and Richie (1999) used the position of the minimum pressure to represent the TC center. Once the horizontal resolution of numerical models is on the order of 1 km, the detailed inner-core processes are resolved and thus the LE methods tend to track the centers of mesoscale vortices in the eye rather than the storm-scale center (Cram et al. 2007). One possible way for solving the problem is to smooth the selected field before detecting the center position (Stern and Zhang 2013).

97 The other two categories are called weighted grid point (WGP) and minimization
98 of azimuthal variance (MAV), respectively. When detecting the pressure or PV centroid,
99 the grid point in the WGP category is weighted by the value of the selected variable
100 (Reasor and Montgomery 2001; Riemer et al. 2010; Ryglicki and Hart 2012; Nguyen
101 et al. 2014). The methods in the MAV category seek to minimize the variance or
102 maximize the mean of a given quantity (Ryglicki and Hart 2015). For example, Braun
103 (2002) and Braun et al. (2006) iterated over grid points in the inner-core region and
104 calculated the azimuthally averaged variance of the pressure field over all radii, looking
105 for the center position with the minimum azimuthally averaged variance. The methods
106 that maximize the tangential wind at the radius of maximum wind were also used in
107 observational and numerical studies (Marks et al. 1992; Wu et al. 2006; Reasor et al.
108 2013).

109 Ryglicki and Hart (2015) analyzed 11 variations of the center-detecting methods in
110 the three categories using four TC forecasts from three operational models. After
111 comparing the spread of the detected centers, the decomposed tangential and radial
112 winds, and the vertical tilt of the TC vortex, they found that the tangential wind
113 differences are generally small and localized, while the vertical tilt derived from the
114 mass field is smallest. Ryglicki and Hodyss (2016) further conducted an analysis of
115 possible errors and inconsistencies in the decomposition of the TC symmetric and
116 asymmetric components, suggesting that the methods that seek to maximize the
117 symmetric component should be chosen when quantities are decomposed in cylindrical
118 coordinates.

In these previous studies mentioned above, the center-detecting methods were evaluated mainly by focusing on the center position relative to storm-scale strong cyclonic flow, track smoothness on an hourly time scale, vertical coherence of the vortex tilt, sensitivity to the model horizontal resolution, and differences in the decomposed symmetric and asymmetric components (Nguyen et al. 2014; Ryglicki and Hart 2015; Ryglicki and Hodyss 2016). In addition to these matrices, we think that an effective method should detect the TC center position that also leads to smooth, consistent evolution in the small-scale track oscillation or trochoidal motion that was confirmed in observations (Jordan 1966; Lawrence and Mayfield 1977; Willoughby 1988; Itano et al. 2002; Hong and Chang 2005) and in numerical simulations (Liu et al. 1999; Wu and Chen 2006). Moreover, the evolution of the vortex tilt is important in the diagnostic analyses of the inner-core dynamic processes of TCs. It is conceivable that the evolution of the small-scale track oscillation and vortex tilt should be smooth and consistent especially for strong TCs in the output of the numerical simulation at a time interval shorter than one hour.

The objective of this study is to reexamine the center-detecting methods that are most frequently used in the WGP and MAV categories by focusing on the evolution of the small-scale track oscillation and vortex tilt, as well as the decomposition of the symmetric and asymmetric components of TC circulation. The data used in this study is a 72-h numerical prediction of Hurricane Wilma (2005) at the 5-minute interval (Chen et al. 2011). Hurricane Wilma (2005) was the most powerful hurricane ever recorded in the Atlantic basin. The lowest minimum sea level pressure was 882 hPa and

its strongest maximum wind speed was greater than 80 m s^{-1}. The data of the predicted Hurricane Wilma and the selected center-detecting methods are described in sections 2 and 3. Section 4 presents the differences among the center-detecting methods, followed by a summary in section 5.

2. The Data of the predicted Hurricane Wilma

The predicted data of Hurricane Wilma (2005) used in this study are from Chen et al. (2011). The detailed setup of the Weather Research and Forecast (WRF) model and the corresponding verification can be referred to Chen et al. (2011). The 72-h prediction was initialized at 0000 UTC 18 October 2005 and terminated at 0000 UTC 21 October 2005, covering an initial 18-h spin-up, an 18-h rapid intensification process, and a 36-h weakening stage with an eyewall replacement process. The initial and lateral boundary conditions were interpolated from then-operational GFDL model data. There were four interactive domains with the horizontal grid spacing of 27 km, 9 km, 3 km and 1 km, respectively, with 55 levels in the vertical. In this study, we mainly use the output of the innermost domain with a horizontal resolution of 1 km, covering an area of 450×450 km. The model output is interpolated into the z-coordinates at 5-minute intervals.

Figure 1 shows the comparisons of the track and intensity from the best track dataset with the prediction after the first 12-hour spin-up. As mentioned in Chen et al. (2011), the model predicted the general northwestward movement of the hurricane although the predicted storm moved faster than the observation during the first 24 h (Fig. 1a). The model predicted the initial spin-up by 18 h, the rapid intensification from

18 h to 36 h and the intensity change associated with the eyewall replacement during the last 36 hours, which are generally consistent with the observation (Fig. 1b). The predicted strongest intensity is 72 m s^{-1} in the near-surface maximum wind speed and 889 hPa in the minimum sea level pressure, which are 10 m s^{-1} and 7 hPa weaker than the observation.

Figure 2 shows the simulated radar reflectivity by 18, 36 and 53 h. The selected three times represent the ending time of the initial spin-up, rapid intensification and eyewall replacement. After the spin-up stage (Fig. 2a), the radar reflectivity exhibits an asymmetric structure with the strongest convection to the south of the storm center. The radius of maximum wind is about 20 km and spiral rainbands can be clearly seen outside the closed eyewall. When the predicted storm reaches the peak intensity (Fig. 2b), the storm structure became more symmetric than that during the spin-up period although the strongest eyewall convection was still located in the southern quadrant. The radius of maximum wind decreases to 17 km when the predicted hurricane reaches its peak intensity at 36 h. At about 60 km from the TC center, there is a nearly-closed rainband, which evolves into the outer eyewall at 53 h (Fig. 2c). The radius of maximum wind increases to 59 km at 53 h.

3. Description of center detection methods

As mentioned in Section 1, the WGP and MAV methods were suggested in the core-resolving numerical simulation. We select four center-detecting methods in the WGP and MAV categories, which have been often used in the analysis of numerical simulations with the horizontal spacing of ~1 km. Three of them are included in Nguyen

et al. (2014). The TC centers detected with the three methods are called the pressure centroid center (PCC), the PV centroid center (PVC) and the maximum tangential wind center (MTC).

The PCC is defined on a constant height surface and the minimum pressure location is used as the first guess. Following Nguyen et al. (2014), the PCC is calculated over a circle of radius *R* as follows:

$$\bar{x} = \frac{\sum_{r=0}^{r=R} x_i P'_i}{\sum_{r=0}^{r=R} P'_i} \quad (1)$$

$$\bar{y} = \frac{\sum_{r=0}^{r=R} y_i P'_i}{\sum_{r=0}^{r=R} P'_i} \quad (2)$$

$$P'_i = P_{env} - P_i \quad (3)$$

where $\bar{x}$ and $\bar{y}$ represent the longitude and latitude of the center; x_i and y_i are the location of the grid point within the circle and P_i' is the pressure perturbation relative to the specified environmental pressure P_{env}. As suggested by Nguyen et al. (2014), the radius of the circle is initially set to 100 km. The resulting latitude and longitude are then used as the next guess and then R is set to two times of R80, i.e., the radius of 80% maximum azimuthally averaged tangential wind at 2 km. The procedure is repeated until there is little change in the calculated center location. In our study, P_{env} is the pressure averaged over the innermost domain.

The detection of the PVC is similar to that of the PCC by replacing the pressure deficit with PV in Eqs. (1) and (2). In this study, we use the grid points with positive PV and R is set to 90 km, including the inner core region of the hurricane. We compared the results of only using positive PV with that of using both positive and negative PV and found that the results are very similar. The sensitivity to the selection of R is

examined and it is found that there is little change in the resulting center location when R is larger than 90 km, about two times of the radius of maximum wind of the outer eyewall.

In the detection of the MTC, the azimuthal mean tangential wind is first calculated by selecting the TC center at each grid point within the eye. The search area is within a circle of 15 km radius in this study. The grid point with the maximum tangential wind is selected as the next guess. The search radius of the circle centered at the new guess is decreased by 50% and the wind field is interpolated to a finer grid with 50% of the initial grid spacing. The procedure continues until the required accuracy of the center location is reached.

The method for detecting the MVC is as follows. The minimum pressure center is selected as the first guess and the azimuthally averaged variance of the pressure field is calculated over all radii between the center and the outer portion of the eyewall. In this study the largest radius is 90 km. Similar to the calculation of the MTC, the azimuthally averaged variance of the pressure field is calculated at each grid point in the eye area. The grid with the minimum azimuthally averaged variance is the next guess. Then the search radius decreases and the pressure field is interpolated to the finer grid points with 50% of the initial grid spacing. The procedure continues until the required accuracy of the center location reaches. Using these four methods, the center positions are detected for each 5-minute interval.

4. Differences of the four detection methods

a. Small-scale track oscillations

In this study, the small-scale track oscillation or trochoidal motion is defined by removing the 9-hour running mean track (Wu and Chen 2016). Comparing to the previous studies (Liu et al. 1999; Nguyen et al. 2014; Ryglicki and Hart 2015; Ryglicki and Hodyss 2016), the differences in the center position or track are much small because of the strong intensity of the predicted TC. This is reflected in both the mean track and the resulting small-scale track oscillation. The mean track exhibits little difference among the four methods (figure not shown). Fig. 3 shows comparisons of the small-scale oscillation, indicating that the four methods lead to very similar track oscillations with the amplitude less than 10 km.

We further examine the small-scale track oscillation by plotting the oscillating tracks derived from the four methods. The oscillating track generally contains two types of cyclonic rotations. One is around the mean track and the other is embedded in the first one with a smaller scale. Fig. 4 shows an example of the oscillating track during 12-20 h. The four methods all lead to a cyclonic rotation around the mean track. The MVC leads to a relatively smooth cyclonic rotation around the mean track and embedded rotations can be identified: one between 12 and 14 h and two between 15 and 17 h (Fig. 4a). The two between 15 and 17 h can be barely detected. The cyclonic rotation around the mean track can be seen in the MTC (Fig. 4b), but erratic or abrupt changes exist, especially for the embedded rotations. Compared to the MVC, the embedded rotations in the PCC are obviously amplified in magnitude (Fig. 4c). The oscillating track of the PVC is similar to that in the MVC, while the embedded rotations are amplified in magnitude (Fig. 4d), compared to Fig. 4a. Fig. 5 shows the oscillations

during 48-60 h. While the oscillating track of the MTC contains many abrupt changes, the other three methods lead to the similar oscillating pattern. As shown in Fig. 4, the oscillating track derived from the MVC are the smoothest one. We also examine the small-scale oscillations during other periods and find that the MVC leads to the smoothest oscillating track relative to the 9-h running mean track.

Why are the embedded oscillations amplified for the PCC? Considering the short period of the embedded oscillation, we examine the 3-km wind, PV and pressure fields at a 10-minute interval from 15 h 50 min to 16 h 40 min (Fig. 6), in which the locations of the MVC, MTC, PCC and PVC are also plotted. The embedded rotation corresponds to the one in the northwest quandrant in Fig. 4. We can see that the pressure minimum is obviously shifted to the eyewall that is indicated by the strong cyclonic winds and strong positive PV anomalies. The center of the pressure minimum rotates cyclonically with a period of about 50 minutes. This suggests that the amplified oscillation is associated with the cyclonic rotation of the pressure minimum.

Careful examination of Fig. 6 indicates that the rotation of the pressure minimum is accompanied by the strong positive PV anomaly that is pooled into the eye region. Zhang et al. (2011) also showed the generation of subvortices inside a major vortex during the initial spin-up period. In a barotropic framework, Schubert et al. (1999) found that barotropic instability made the vorticity of the eyewall region be pooled into the eye region and suggested that the observed polygonal eyewalls or mesovortices may be due to vorticity mixing. Kossin and Schubert (2001) further found that the vorticity mixing can significantly decrease the pressure in the eye region. Moreover, Stern and

Zhang (2013) confirmed that the eddy advection of potential temperature dominated by the wavenumber-1 component can lead to the mid-level warming in the eye, which can lower the low-level pressure. Although further in-depth investigation is needed, Fig. 6 suggests that the pressure minimum is associated with the PV mixing in the eye region, which makes the pressure minimum closer to the eyewall and amplifies the embedded oscillation of the PCC in magnitude.

To further demonstrate the effect of PV mixing, we calculate the mean track from the four methods at one-hour intervals and obtain their deviations from the mean track at 3-km altitude (Fig. 7). The deviations actually measure the spread of the center position relative to the mean track. Compared to Nguyen et al. (2014) and Ryglicki and Hart (2015), it is expected that the deviations of the center positions detected by the four methods are generally small, less than 4 km in the zonal and meridional directions. In particular, the deviations are smaller during the rapid intensification period (18-36 h) than those during the initial spin-up period and the eyewall replacement process, when the radius of maximum wind is relatively larger. Note that there is a systematic bias in the differences shown in Fig. 7, which can be clearly seen after a 9-hour running mean is applied to the time series. The PCC bias is consistent with that of the PVC, which is generally located to the northeast of the MVC and MTC. The consistence further indicates the effect of PV mixing on the embedded oscillation of the PCC.

b. Vortex tilt

Although it tends to maintain an upright structure (Wu and Wang 2001a, b; Reasor et al. 2013), the TC-scale vortex often tilts in the vertical, in particular due to the

influence of vertical shear of the environmental flow (Jones 1995; Frank and Richie 1999). In the previous studies (e. g., Nguyen et al. 2014; Ryglicki and Hart 2015), the vertical tilt is measured with the relative shift of the vortex center between two levels. Here the vertical tilt is defined using the difference of the center position between 1 km and 8 km. Fig. 8 shows the direction and magnitude of the vertical tilt from the four different methods. The vertical tilt can be larger than 12 km during the spin-up stage and decreases rapidly by the onset of the rapid intensification. The tilt magnitude remains within 2 km during the rapid intensification and then increases during the eyewall replacement process. The increasing tilt from 32 h to 48 h coincides with the weakening of the TC intensity (Fig. 1b). The TC intensifies after the eyewall replacement and the vertical tilt increases by 72 h. We can see that the tilt magnitude remains within 6 km after the initial spin-up. Further examination indicates that the changes of the tilt magnitudes are generally consistent with the evolution of the vertical wind shear (figure not shown), but the vertical tilt based on the MTC is most sensitive to the shear change.

A striking feature in Fig. 8 is the considerable fluctuations in both the direction and magnitude of the vertical tilt. The mean and variance of the vertical tilt are calculated for each method. The mean vertical tilt and variance derived from the MVC (PVC) is smallest (largest) in magnitude. We also examine the vertical tilts between 1 km and 5 km and between 1 km and 12 km (not shown). Similar to the vertical tilt between 1 km and 8 km, the MVC leads to the smallest vertical tilt in the two layer, suggesting that the predicted TC maintains a vertically coherent structure.

317 The fluctuations in the direction and magnitude can be futher demonstrated by
318 plotting the 8-km level track relative to the 1-km level track. Fig. 9 shows the relative
319 tracks for the MVC, MTC, PCC and PVC during the periods 16-20 h, 42-46 h and 54-
320 58 h. The selected periods correspond to the ending time of the spin-up, post rapid
321 intensification stage, and eyewall replacement. For clarity, the zonal and meridional
322 scales vary in different panels. The relative tracks of the MVC and PVC are generally
323 smooth, but the pattern and magnitude are different between the MVC and PVC, with
324 larger vertical tilt for the PVC. The relative tracks of the PCC and PVC contain abrupt
325 changes. In particular, the fluctuations in the MTC are generally in a zigzag nature.
326 Figure 9 indicates that the relative tracks also contain cyclonic rotations. The
327 fluctuations of the vertical tilt have not confirmed in the observation. Considering that
328 the TC vortex is not a solid object, we think that it is not surprising that vortex vertical
329 tilt fluctuates in time. Since the predicted Wilma is a very intense hurricane, the abrupt
330 changes on such a short time scale should be unrealistic and unphysical. Fig. 9 suggests
331 that the MVC and PVC exhibit a good performance in the vertical tilt. It should be
332 mentioned that the vertical wind shear in the case is small and we cannot find a clear
333 relationship between the vertical tilt and the vertical wind shear.
334 **c. Symmetric and asymmetric circulations**
335 As mentioned above, the relatively larger differences in the detected center position
336 occur during the initial spin-up period, while the smallest differences are during the
337 rapid intensification. To demonstrate the influence of the center location on the
338 decomposed circulations of the predicted Hurricane Wilma, we compare the symmetric

and asymmtric circulations at 18, 36 and 53 h, respectively. For convenience, we compare the symmetric structure resulting from the PCC, PVC and MTC with that based on the MVC. Since the differences at 36 and 53 h are much smaller than those at 18 h, we show only the differences at 18 h. Note that the decomposition is based on the center detected at each vertical level.

Figure 10a shows the azimuthally averaged tangential wind based on the MVC at 18 h. In this figure we also plot the radius of maximum wind (RMW) at each altitude. Note that the zigzag feature of the RMW results from the 1-km vertical resolution of the interpolated model output. The maximum tangential wind exceeds 50 m s^{-1} and the RMW tilts radially outward below 14 km. Figs. 10b-d show the differences of the azimuthally averaged tangential wind based on the MTC, PCC and PVC from that based on the MVC. For clarity, note that the scales of the shading in Figs. 8b-d are different. The MTC leads to the maximum difference of about 0.5 m s^{-1} in the symmetric component of tangential wind, which is much smaller than the PCC and PVC. Since the MTC is identified to maximize the symmetric component of tangential wind, we conclude that the MVC can also maximize the symmetric component of tangential wind. Compared to the MTC, the symmetric component of tangential wind derived from the PCC and PVC is weaker near the RMW. The maximum reduction is about 7 m s^{-1} for the PCC and 3.5 m s^{-1} for the PVC. We also compare the differences of the azimuthally averaged radial wind at 18 h and find that the PCC and PVC lead to relatively larger differences (figure not shown).

The differences in the symmetric component can lead to differences in the asymmetric component. Fig. 11 shows the asymmetric wind fields in the inner core region at 3 km. As expected, the asymmetric flows based on the MVC and MTC are weaker than those from the PCC and PVC. The maximum asymmetric winds exceeding 20 m s^{-1} for the PCC and 12 m s^{-1} for the PVC can be found within the RMW. Compared to the MVC and MTC, the MVC and MTC lead to the very similar symmetric structure in the tangential wind, while the PCC and PVC result in the reduced tangential wind near the RMW and strong asymmetric winds in the eye region.

Figure 12a shows the radius-height cross section of the symmetric component of PV from the MVC at 18 h. We can see large positive PV at the middle levels inside the RMW. Figs. 12b-d show the corresponding differences from those derived from the MTC, PCC and PVC. Note that the scales of the shading are also different in the figures. The intensities of the symmetric PV component derived from the MTC, PCC and PVC are weaker than that from the MVC. The reduction of the PV intensity is significant for the PCC and PVC. For PCC (PVC), the PV intensity at the middle levels can be reduced by 50% (30%), while it decreases by less than 10% for the MTC. Moreover, the positive and negative pattern of the PV difference in Figs. 12b-d suggests that the radial PV gradient in the eyewall region is reduced, especially for the PCC and PVC.

5. Summary

In this study, the 1-km resolution output of the predicted Hurricane Wilma (2005) at 5-minute intervals is used to evaluate the PCC, PVC, MTC and MVC, which are frequently used in the diagnostic analysis of the inner-core dynamics processes.

Hurricane Wilma (2005) was the most powerful hurricane ever recorded in the Atlantic basin. We assume that the small-amplitude track oscillation and the fluctuations of the vortex tilt should evolve smoothly and consistently. Our focus is placed on the evolution of the small-scale track oscillation and vortex tilt.

Compared to the previous studies (Nguyen et al. 2014; Ryglicki and Hart 2015), the differences in the detected center position and vertical tilt are generally small during the rapid intensification and eyewall replacement due to the strong TC intensity. The four methods all lead to similar small-scale track oscillations that rotate cyclonically around the mean track. While the MVC and PVC leads to a relatively smooth rotation, abrupt changes exist in the track oscillation of the MTC; the track oscillation of the PCC contains amplified embedded rotations that are associated with the PV mixing in the eye region. The tracks of the MVC and PVC relative to the lower-level center (vertical tilt) are generally smooth, while the relative tracks of the MTC and PCC contain abrupt changes. The MVC leads to the strongest symmetric structure in the tangential wind, PV, and radial PV gradient in the eyewall region. Although this study is only based on a single case, it is suggested that the MVC should be selected in the study of the inner-core processes.

In this study, the predicted Wilma has a well-developed structure and a single case study is provided. It should be noted that the conclusions may be affected by the size of the storm eye, the strength of the storm, the underlying topography (e.g. islands with high altitude topography), and even the depth of the storm. Therefore, further investigation is needed in the future.

Acknowledgments The detail of the predicted data of Hurricane Wilma (2005) was described in Chen et al. (2011). The authors thank Prof. Da-Lin Zhang of University of Maryland for providing the prediction data. The research was jointly supported by the National Basic Research Program of China (2015CB452803), and the National Natural Science Foundation of China (NSFC No. 41730961, No. 41675051).

References

Braun, S. A., 2002: A cloud-resolving simulation of Hurricane Bob (1991): Storm structure and eyewall buoyancy. *Mon. Wea. Rev.*, **130,** 1573–1592.

Braun, S. A., M. T. Montgomery, and Z. Pu, 2006: High-resolution simulation of Hurricane Bonnie (1998). Part I: The organization of eyewall vertical motion. *J. Atmos. Sci.*, **63,** 19–42.

Bryan, G. H., D. P. Stern, and R. Rotunno, 2014: A Framework for Studying the Inner Core of Tropical Cyclones Using Large Eddy Simulation, *31st Conf. on Hurricanes and Tropical Meteorology*, San Diego, CA., Amer. Meteor. Soc.

Cavallo, S. M., R. D. Torn, C. Snyder, C. Davis, W. Wang, and J. Done, 2013: Evaluation of the Advanced Hurricane WRF data assimilation system for the 2009 Atlantic hurricane season. *Mon. Wea. Rev.*, **141,** 523–541.

Chen, H., D.-L. Zhang, J. Carton, and R. Atlas, 2011: On the rapid intensification of Hurricane Wilma (2005). Part I: Model prediction and structural changes. *Wea. Forecasting*, **26,** 885–901.

426 Cram, T. A., J. Persing, M. T. Montgomery, and S. A. Braun, 2007: A Lagrangian
427 trajectory view on transport and mixing processes between the eye, eyewall, and
428 environment using a high-resolution simulation of Hurricane Bonnie (1998). *J.*
429 *Atmos. Sci.*, **64,** 1835-1856.
430 Frank, W. M., and E. A. Ritchie, 1999: Effects of environmental flow upon tropical
431 cyclone structure. *Mon. Wea. Rev.*, **127,** 2044-2061.
432 Green, B. W., and F. Zhang, 2015: Numerical simulations of Hurricane Katrina (2005)
433 in the turbulent gray zone. *J. Adv. Model. Earth Syst.*, **7,** 142–161.
434 Hong, J.-S., and P.-L. Chang, 2005: The trochoid-like track in Typhoon Dujuan
435 (2003). *Geophys. Res. Lett.*, **32,** L16801.
436 Itano, T., G. Naito, and M. Oda, 2002: Analysis of elliptical eye of Typhoon Herb
437 (T9609) (in Japanese with English abstract). *Sci. Eng. Rep. Natl. Def.*
438 *Acad.*, **39,** 9–17.
439 Jones, S. C., 1995: The evolution of vortices in vertical shear. I: Initially barotropic
440 vortices. *Quart. J. Roy. Meteor. Soc.*, **121,** 821-851.
441 Jordan, H. M., and D. J. Stowell, 1955: Some small scale features of the track of
442 Hurricane Ione. *Mon. Wea. Rev.*, **83,** 210–215.
443 Jordan, C. L., 1966: Surface pressure variations at coastal stations during the period of
444 irregular motion of Hurricane Carla of 1961. *Mon. Wea. Rev.*, **94,** 454–458.
445 Kossin, J. P., and W. H. Schubert, 2001: Mesovortices, polygonal flow patterns, and
446 rapid pressure falls in hurricane-like vortices. *J. Atmos. Sci.*, **58,** 2196–2209.

Lawrence, M. B., and B. M. Mayfield, 1977: Satellite observations of trochoidal motion of Hurricane Bell 1976. *Mon. Wea. Rev.,* **105,** 1458–1461.

Liu, Y., D.-L. Zhang, and M. K. Yau, 1999: A multiscale numerical study of Hurricane Andrew (1992). Part II: Kinematics and inner-core structures. *Mon. Wea. Rev.,* **127,** 2597–2616.

Marks Jr, F. D., R. A. Houze Jr, and J. F. Gamache, 1992: Dual-aircraft investigation of the inner core of Hurricane Norbert. Part I: Kinematic structure. *J. Atmos. Sci.*, **49,** 919-942.

Montgomery, M. T., and R. J. Kallenbach, 1997: A theory for vortex Rossby waves and its application to spiral bands and intensity changes in hurricanes. *Quart. J. Roy. Meteor. Soc*, **123,** 535–565.

Nguyen, L. T., J. Molinari, and D. Thomas, 2014: Evaluation of tropical cyclone center identification methods in numerical models. *Mon. Wea. Rev.*, **142,** 4326–4339.

Reasor, P. D., and M. T. Montgomery, 2001: Three-dimensional alignment and corotation of weak, TC-like vortices via linear vortex Rossby waves. *J. Atmos. Sci.*, **58,** 2306–2330.

Reasor, P. D., R. F. Rogers, and S. Lorsolo, 2013: Environmental flow impacts on tropical cyclone structure diagnosed from airborne Doppler radar composites. *Mon. Wea. Rev.,* **141,** 2949–2969.

Riemer, M., M. T. Montgomery, and M. E. Nicholls, 2010: A new paradigm for intensity modification of tropical cyclones: Thermodynamic impact of vertical wind shear on the inflow layer. *Atmos. Chem. Phys.*, **10,** 3163-3188.

Rotunno, R., Y. Chen, W. Wang, C. Davis, J. Dudhia, and G. J. Holland, 2009: Large-eddy simulation of an idealized tropical cyclone. *Bull. Amer. Meteor. Soc.*, **90,** 1783–1788.

Rotunno, R., and G. H. Bryan, 2014: Effects of resolved turbulence in a large eddy simulation of a hurricane, *31st Conf. on Hurricanes and Tropical Meteorology*, San Diego, CA., Amer. Meteor. Soc.

Ryglicki, D. R., and R. E. Hart, 2012: An investigation of metrics used to determine the center of model tropical cyclones. 30th Conf. on Hurricanes and Tropical Meteorology, Ponte Vedra, FL, Amer. Meteor. Soc., 3A.5.

Ryglicki, D. R., and R. E. Hart, 2015: An investigation of center-finding techniques for tropical cyclones in mesoscale models. *J. Appl. Meteor. Climatol.*, **54,** 825–846.

Ryglicki, D. R., and D. Hodyss, 2016: A deeper analysis of center-finding techniques for tropical cyclones in mesoscale models. Part I: Low-wavenumber analysis. *J. Appl. Meteor. Climatol.*, **55,** 531-559.

Schubert, W. H., M. T. Montgomery, R. K. Taft, T. A. Guinn, S. R. Fulton, J. P. Kossin, and J. P. Edwards, 1999: Polygonal eyewalls, asymmetric eye contraction, and potential vorticity mixing in hurricanes. *J. Atmos. Sci.*, **56,** 1197–1223.

Stern, D. P., and F. Zhang, 2013: How does the eye warm? Part I: A potential temperature budget analysis of an idealized tropical cyclone. *J. Atmos. Sci.*, **70,** 73-90.

Stern, D. P., and G. H. Bryan, 2018: Using Simulated Dropsondes to Understand Extreme Updrafts and Wind Speeds in Tropical Cyclones. *Mon. Wea. Rev.*, **146,** 3901-3925.

Willoughby, H. E., 1988: Linear motion of a shallow-water, barotropic vortex. *J. Atmos. Sci.*, **45,** 1906–1928.

Willoughby, H. E., 1992: Linear motion of a shallow-water barotropic vortex as an initial-value problem. *J. Atmos. Sci.*, **49,** 2015–2031.

Wu, L., and B. Wang, 2001: Movement and vertical coupling of adiabatic baroclinic tropical cyclones. *J. Atmos. Sci.*, **58,** 1801-1814.

Wu, L., and B. Wang, 2001: Effects of convective heating on movement and vertical coupling of tropical cyclones: A numerical study. *J. Atmos. Sci.*, **58,** 3639-3649.

Wu, L., S. A. Braun, J. Halverson, and G. Heymsfield, 2006: A numerical study of Hurricane Erin (2001). Part I: Model verification and storm evolution. *J. Atmos. Sci.*, **63,** 65–86.

Wu, L., and X. Chen, 2016: Revisiting the steering principal of tropical cyclone motion in a numerical experiment. *Atmos. Chem. Phys.*, **16,** 14925–14936.

Zhang, D.-L., L. Tian, and M.-J. Yang, 2011: Genesis of Typhoon Nari (2001) from a mesoscale convective system. Journal of Geophysical Research: Atmospheres, **116**, D23104, https://doi.org/10.1029/2011JD016640.

510 Zhu, P., 2008: Simulation and parameterization of the turbulent transport in the
511 hurricane boundary layer by large eddies. *J. Geophys. Res.*, **113,** D17104.
512
513

514 **Figure Captions**

515 Figure 1 (a) The observed (red) and predicted (blue) tracks of Hurricane Wilma
516 (2005) during the period 1200 UTC 18 October 2005 (12 h) to 0000 UTC 21
517 October 2005 (72 h) and (b) the predicted maximum wind speed (red, m s^{-1}) and
518 minimum sea level pressure (SLP) (blue, hPa).

519 Figure 2 The predicted 3-km radar reflectivity (shading, dBZ) at (a) 18 h, (b) 36 h and
520 (c) 53 h. The plus symbol denotes the position of the tropical cyclone center with
521 arrows indicating the vertical wind shear between 200 hPa and 850 hPa.

522 Figure 3 The zonal (a) and meridional (b) oscillations of the tropical cyclone tracks at
523 z = 3 km derived by removing the 9-hour running mean. The oscillations are
524 based on the PCC (blue), PVC (yellow), MTC (red) and MVC (black).

525 Figure 4 The track oscillations (km) relative to the 9-hour running mean tracks
526 derived from the MVC (a), MTC (b), PCC (c) and PVC (d) at z = 3 km,
527 respectively, during 12 - 20 h. The numbers by open circles are the hours from
528 1200 UTC 18 October 2005.

529 Figure 5 The track oscillations (km) relative to the 9-hour running mean tracks
530 derived from the MVC (a), MTC (b), PCC (c) and PVC (d) at z = 3 km,
531 respectively, during 48 - 60 h. The numbers by filled circles are the hours from
532 0000 UTC 20 October 2005.

533 Figure 6 The wind (vectors, m s^{-1}), PV (shading, PVU) and pressure fields (contour,
534 hPa) at z = 3 km during 1550 UTC and 1640 UTC 18 October 2005. The filled
535 star, circle, triangle and square denote the location of MVC, MTC, PCC and

PVC, respectively.

Figure 7 The zonal (a) and meridional (b) differences of the identified tracks by PCC (blue), PVC (yellow), MTC (red) and MVC (black) from the mean center position averaged with the four center positions at z = 3 km. The thick lines represent the 9-hour running mean of the corresponding time series.

Figure 8 The direction (a) and magnitude (b) of the vertical tilt of the Wilma vortex between 8 km and 1 km during 12 - 72 h, derived from the MVC (black), MTC (red), PCC (blue) and PVC (green). The direction is measured clockwise from due north.

Figure 9 The 8-km center position relative to the center at 1 km during 16 - 20 h, 42 – 46 h and 54 – 58 h, derived from the MVC (a - c), MTC (d - f), PCC (g - i) and PVC (j - l), respectively. The numbers by filled circles are the hours.

Figure 10 The altitude-radius cross section of the azimuthal mean tangential wind (shading, m s^{-1}) for the MVC (a) and the differences (shading, m s^{-1}) between the azimuthal mean tangential wind based on the MTC (b), PCC (c) and PVC (d) and that based on the MVC at 18 h. The red line indicates the radius of maximum wind for the corresponding center while the black line indicates the radius of maximum wind for the MVC. Note the scales of the shading are different in (b), (c) and (d) for clarity.

Figure 11 The z = 3 km asymmetric wind fields (vectors, m s^{-1}) based on MVC (a), MTC (b), PCC (c) and PVC (d) at 18 h. The shading indicates the magnitude (m s^{-1}) of the asymmetric wind, and the dashed circle denote the radius of maximum

wind for the corresponding center.

Figure 12 The altitude-radius cross section of the azimuthal mean potential vorticity (shading, PVU) for the MVC (a) and the differences (shading, PVU) between the potential vorticity based on the MTC (b), PCC (c) and PVC (d) and that based on the MVC at 18 h. The red line indicates the radius of maximum wind for the corresponding center while the black line indicates the radius of maximum wind for the MVC. Note the scales of the shading are different in (b), (c) and (d) for clarity.

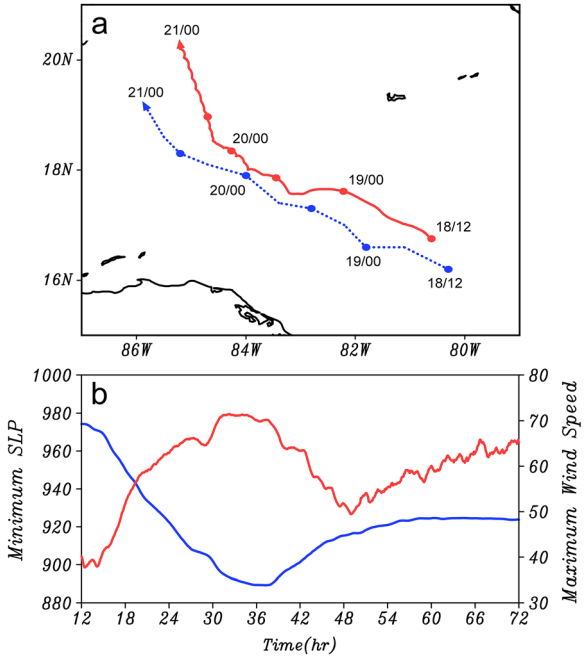

Figure 1 (a) The observed (red) and predicted (blue) tracks of Hurricane Wilma (2005) during the period 1200 UTC 18 October 2005 (12 h) to 0000 UTC 21 October 2005 (72 h) and (b) the predicted maximum wind speed (red, m s^{-1}) and minimum sea level pressure (SLP) (blue, hPa).

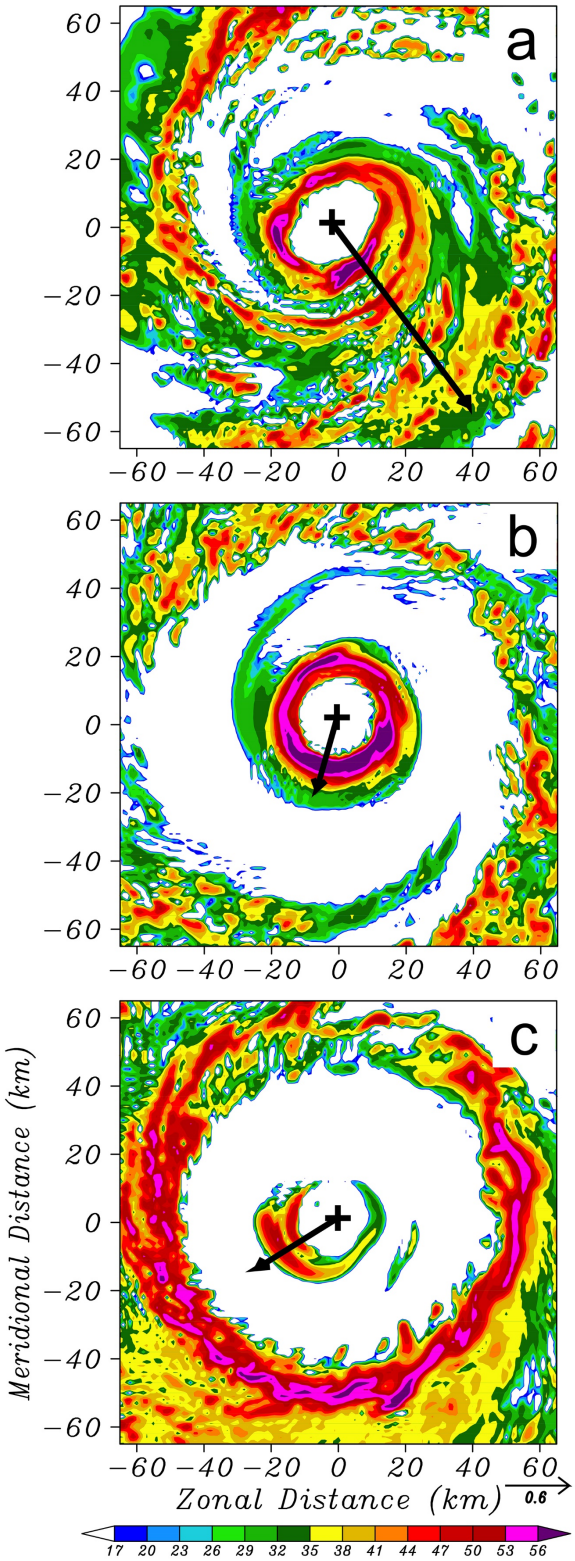

Figure 2 The predicted 3-km radar reflectivity (shading, dBZ) at (a) 18 h, (b) 36 h and (c) 53 h. The plus symbol denotes the position of the tropical cyclone center with arrows indicating the vertical wind shear between 200 hPa and 850 hPa.

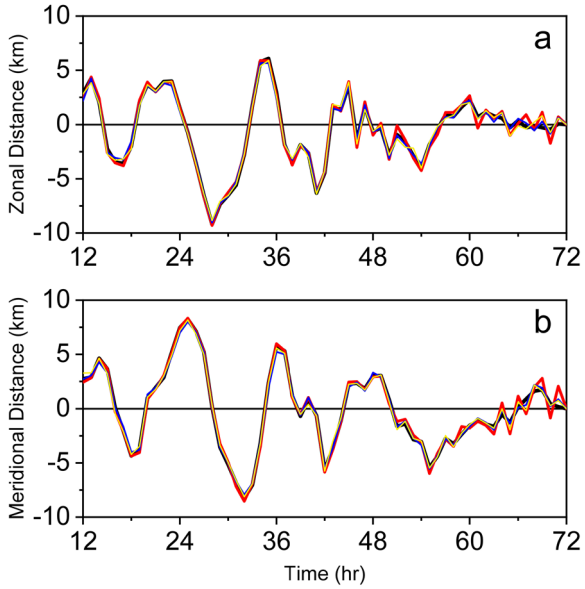

Figure 3 The zonal (a) and meridional (b) oscillations of the tropical cyclone tracks at z = 3 km derived by removing the 9-hour running mean. The oscillations are based on the PCC (blue), PVC (yellow), MTC (red) and MVC (black).

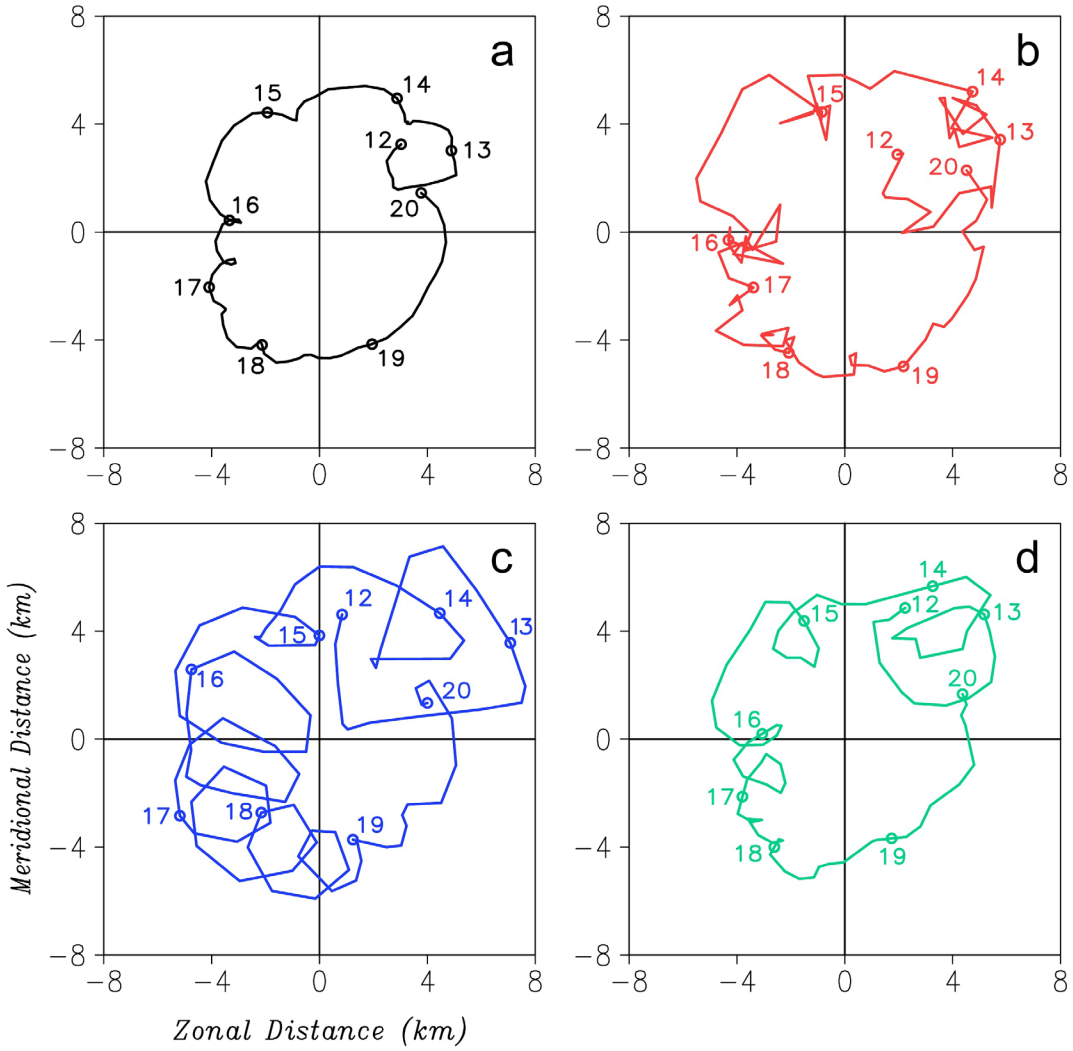

Figure 4 The track oscillations (km) relative to the 9-hour running mean tracks derived from the MVC (a), MTC (b), PCC (c) and PVC (d) at z = 3 km, respectively, during 12 - 20 h. The numbers by open circles are the hours from 1200 UTC 18 October 2005.

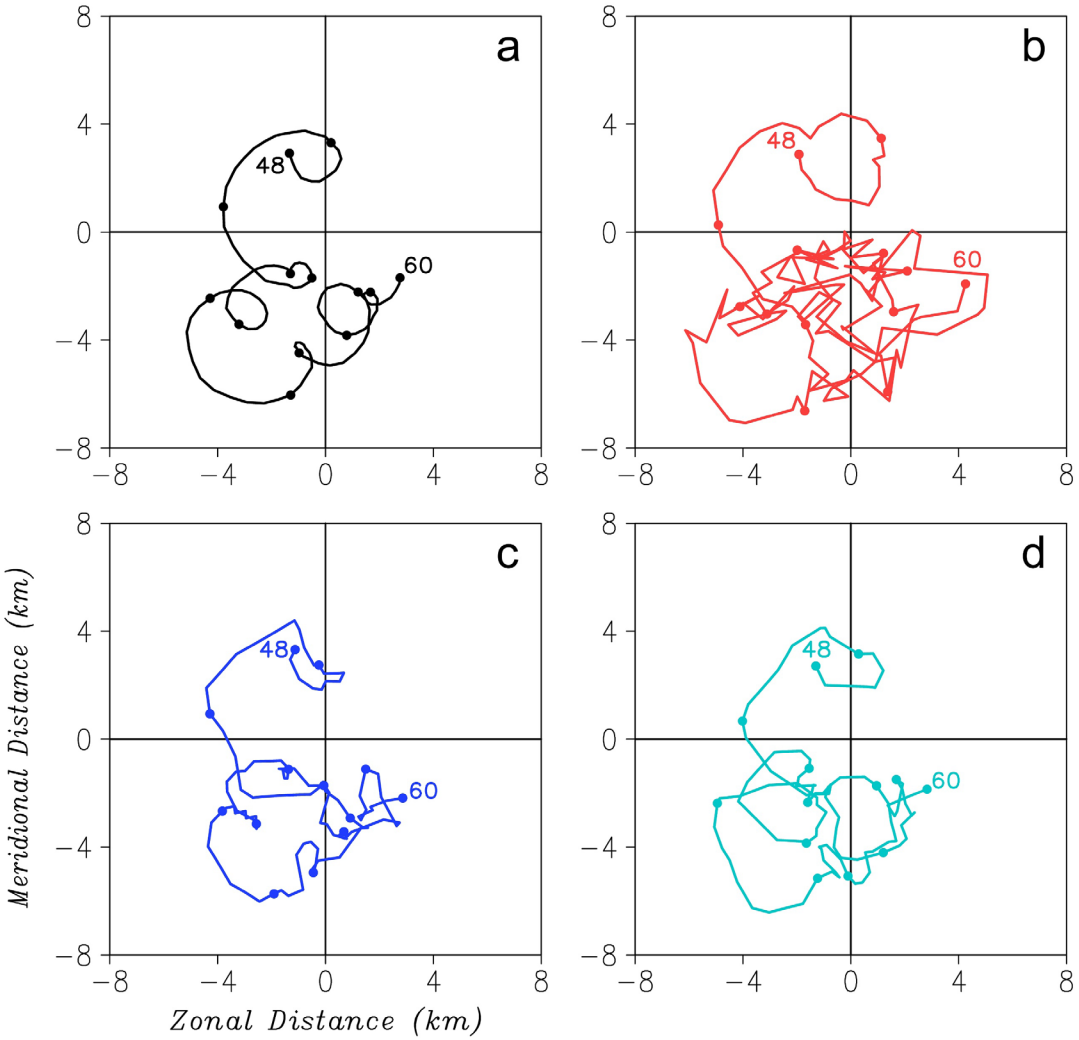

Figure 5 The track oscillations (km) relative to the 9-hour running mean tracks derived from the MVC (a), MTC (b), PCC (c) and PVC (d) at z = 3 km, respectively, during 48 - 60 h. The numbers by filled circles are the hours from 0000 UTC 20 October 2005.

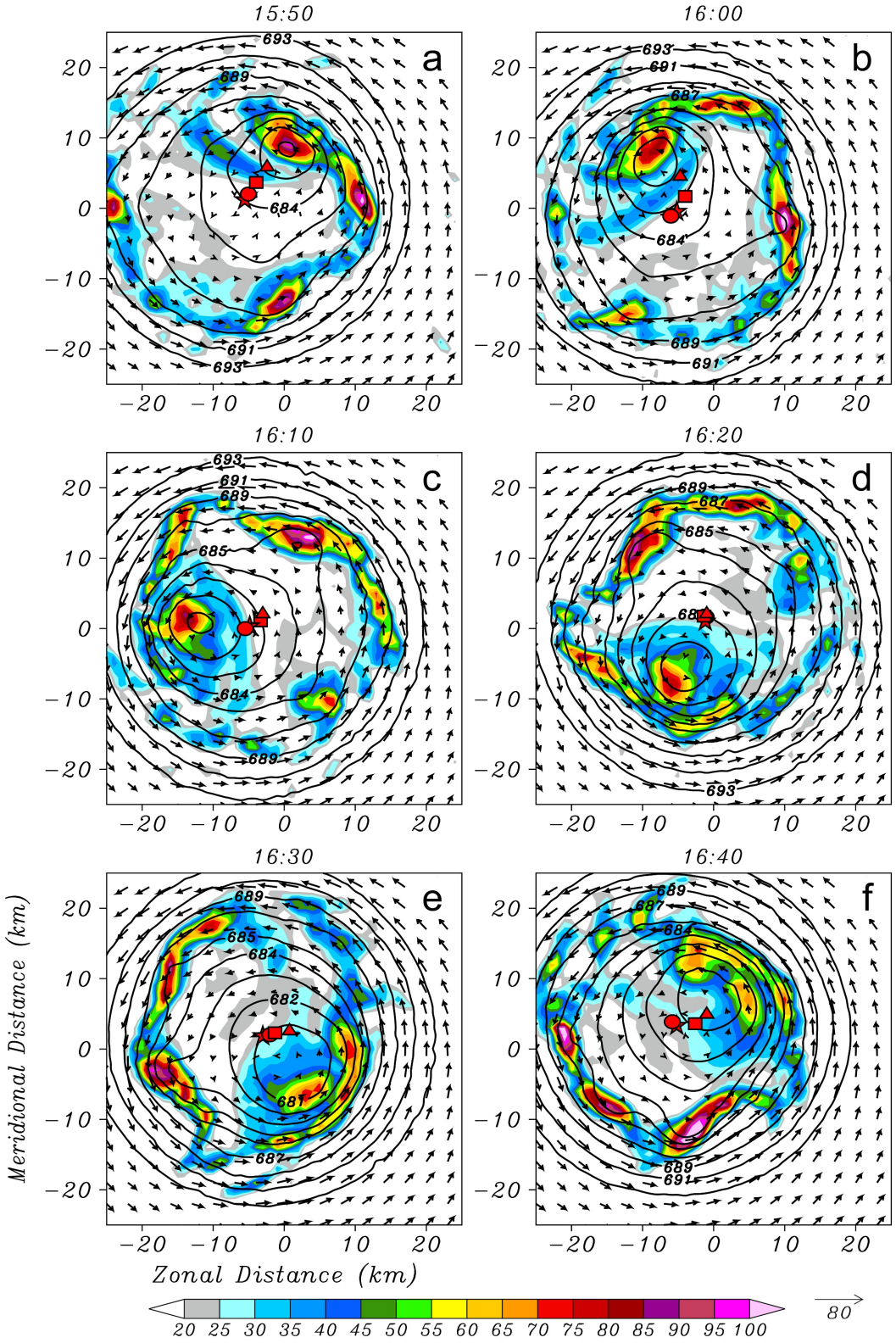

603

604 Figure 6 The wind (vectors, m s^{-1}), PV (shading, PVU) and pressure fields (contour,

605 hPa) at z = 3 km during 1550 UTC and 1640 UTC 18 October 2005. The filled star,

606 circle, triangle and square denote the location of MVC, MTC, PCC and PVC,
607 respectively.

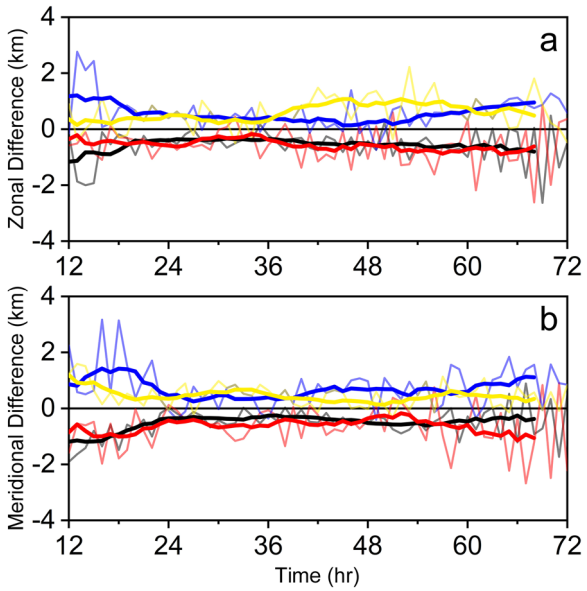

608

609 Figure 7 The zonal (a) and meridional (b) differences of the identified tracks by PCC
610 (blue), PVC (yellow), MTC (red) and MVC (black) from the mean center position
611 averaged with the four center positions at z = 3 km. The thick lines represent the 9-hour
612 running mean of the corresponding time series.
613

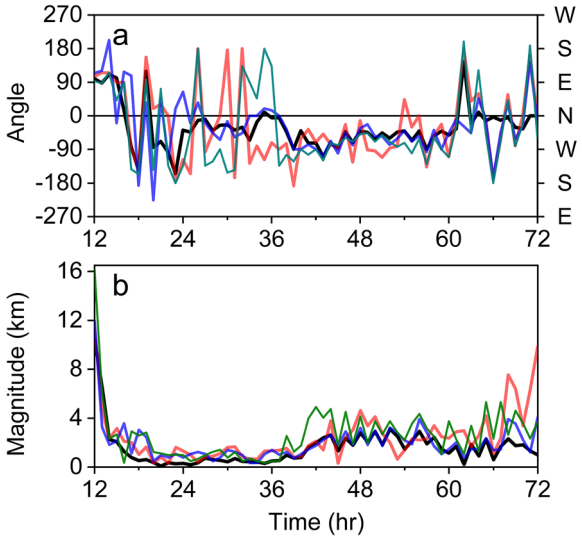

614

615 Figure 8 The direction (a) and magnitude (b) of the vertical tilt of the Wilma vortex
616 between 8 km and 1 km during 12 - 72 h, derived from the MVC (black), MTC (red),
617 PCC (blue) and PVC (green). The direction is measured clockwise from due north.
618

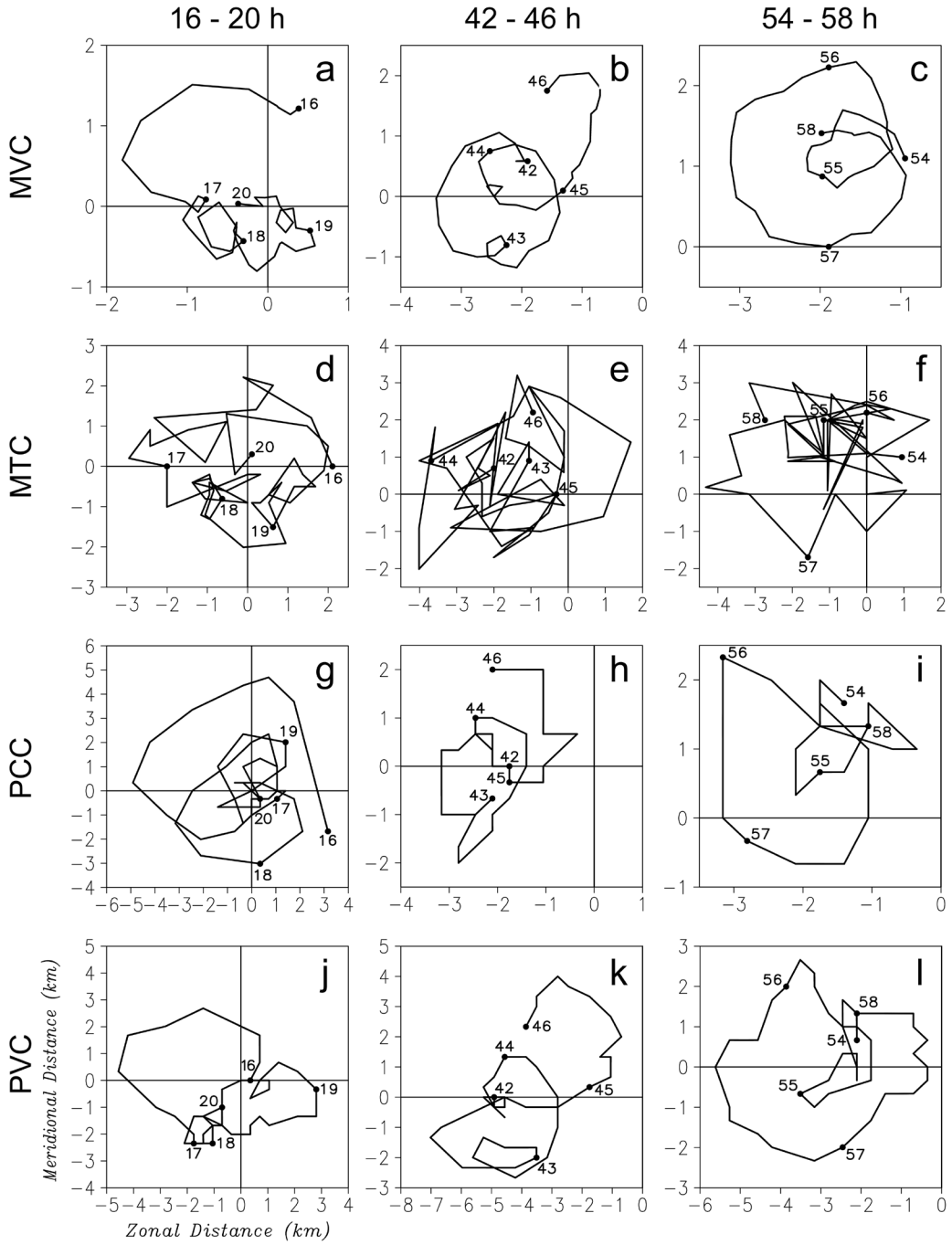

Figure 9 The 8-km center position relative to the center at 1 km during 16 - 20 h, 42 – 46 h and 54 – 58 h, derived from the MVC (a - c), MTC (d - f), PCC (g - i) and PVC (j - l), respectively. The numbers by filled circles are the hours.

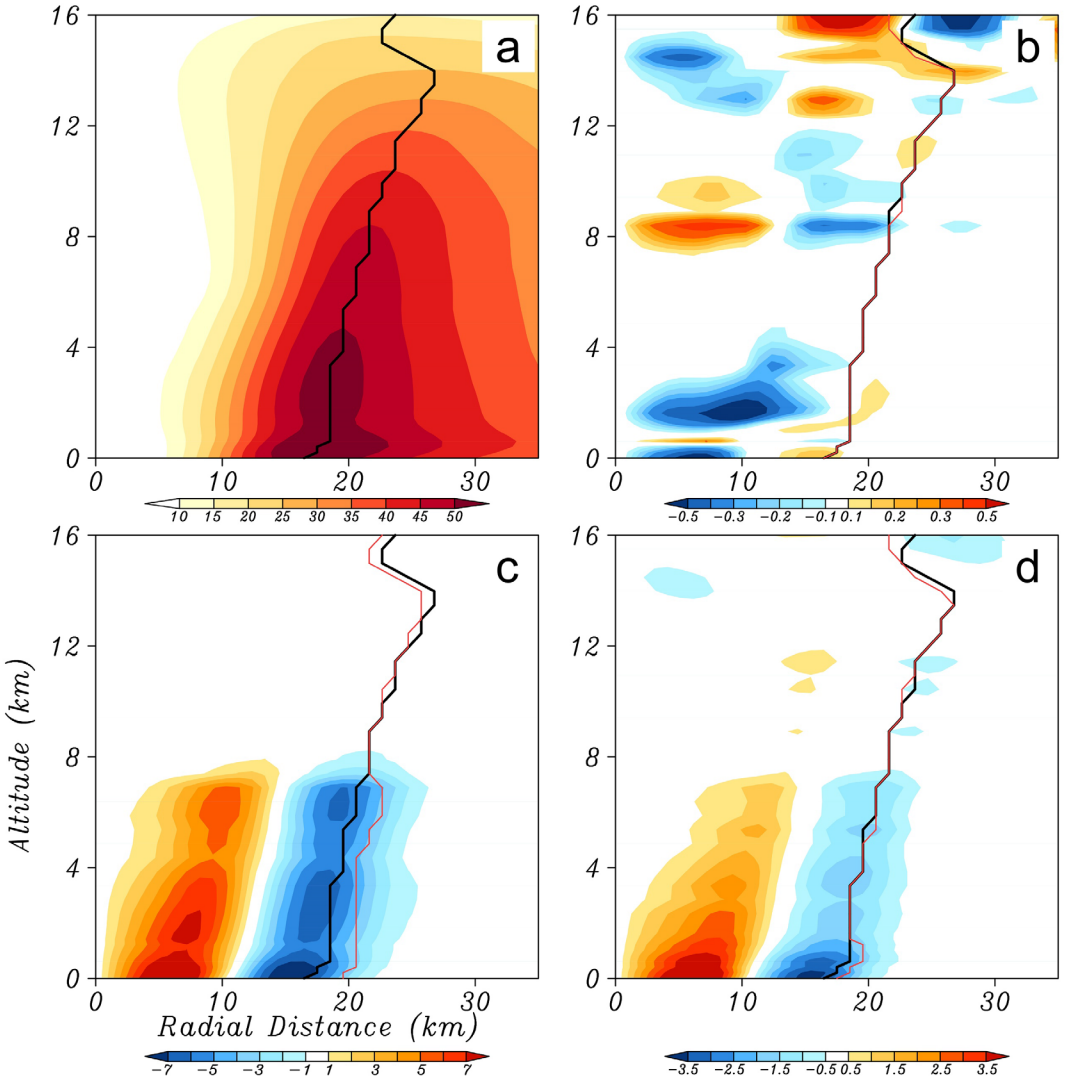

Figure 10 The altitude-radius cross section of the azimuthal mean tangential wind (shading, m s^{-1}) for the MVC (a) and the differences (shading, m s^{-1}) between the azimuthal mean tangential wind based on the MTC (b), PCC (c) and PVC (d) and that based on the MVC at 18 h. The red line indicates the radius of maximum wind for the corresponding center while the black line indicates the radius of maximum wind for the MVC. Note the scales of the shading are different in (b), (c) and (d) for clarity.

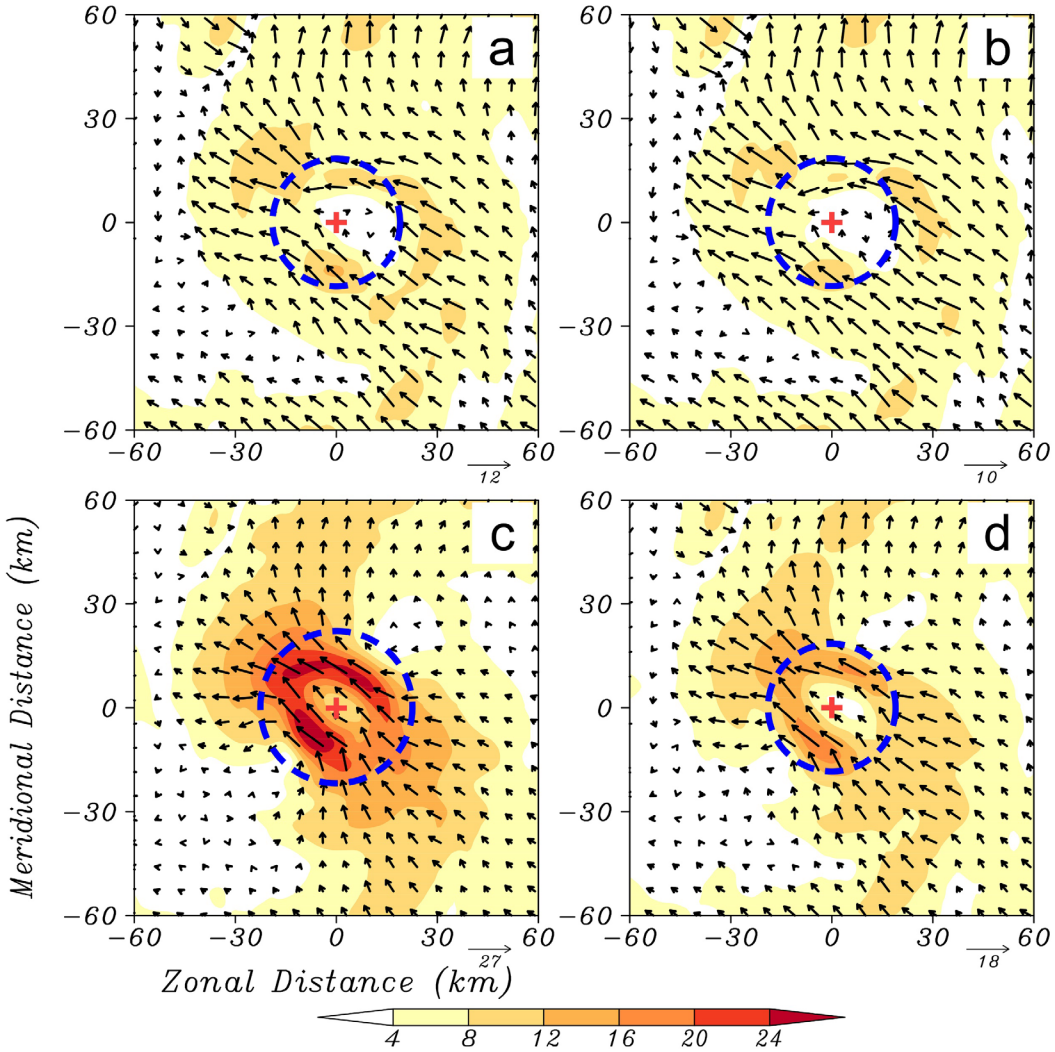

637

638 Figure 11 The z = 3 km asymmetric wind fields (vectors, m s^{-1}) based on MVC (a),

639 MTC (b), PCC (c) and PVC (d) at 18 h. The shading indicates the magnitude (m s^{-1}) of

640 the asymmetric wind, and the dashed circle denote the radius of maximum wind for the

641 corresponding center.

642

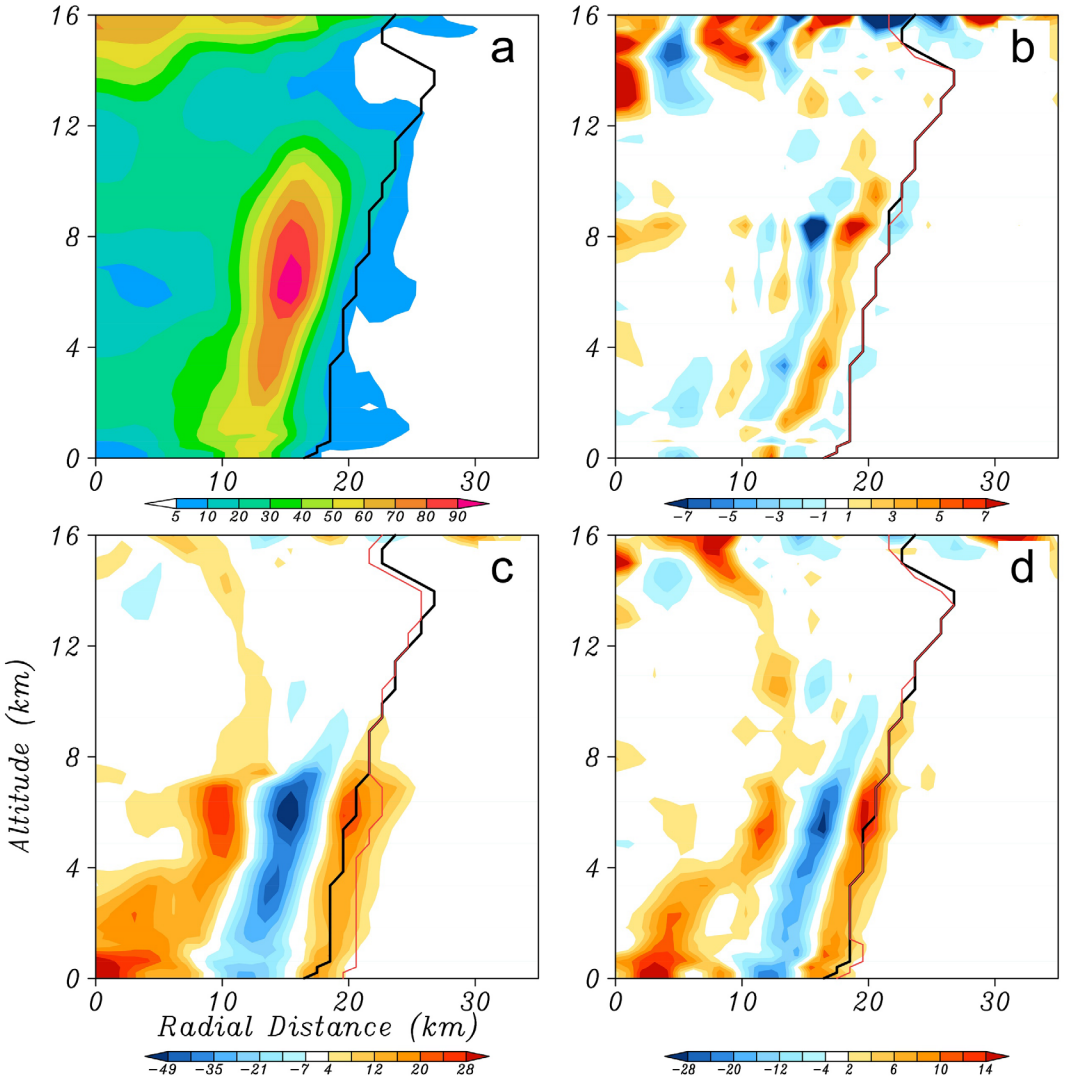

643

644 Figure 12 The altitude-radius cross section of the azimuthal mean potential vorticity
645 (shading, PVU) for the MVC (a) and the differences (shading, PVU) between the
646 potential vorticity based on the MTC (b), PCC (c) and PVC (d) and that based on the
647 MVC at 18 h. The red line indicates the radius of maximum wind for the corresponding
648 center while the black line indicates the radius of maximum wind for the MVC. Note
649 the scales of the shading are different in (b), (c) and (d) for clarity.

650